Atmos. Chem. Phys., 7, 1851–1868, 2007
www.atmos-chem-phys.net/7/1851/2007/

Atmospheric Chemistry and Physics

Mesoscale circulations over complex terrain in the Valencia coastal region, Spain – Part 2: Modeling CO_2 transport using idealized surface fluxes

G. Pérez-Landa[1], P. Ciais[2], G. Gangoiti[3], J. L. Palau[1], A. Carrara[1], B. Gioli[4], F. Miglietta[4], M. Schumacher[5], M. M. Millán[1], and M. J. Sanz[1]

[1]Fundación CEAM. Parque Tecnológico, c/ Charles R. Darwin 14, 46980 Paterna (Valencia), Spain
[2]Laboratoire des Sciences du Climat et de l'Environnement, UMR Commissariat à l'Energie Atomique/CNRS 1572, Gif-sur-Yvette, France
[3]Escuela Técnica Superior de Ingenieros Industriales de Bilbao, Universidad del País Vasco/Euskal Herriko Unibertsitatea, Bilbao, Spain
[4]IBIMET-CNR, Instituto di Biometeorologia, Consiglio Nazionale delle Ricerche, Firenze, Italy
[5]Max-Planck-Institut für Biogeochemie, Hans-Knöll-Strasse 10, 07745 Jena, Germany

Received: 22 December 2005 – Published in Atmos. Chem. Phys. Discuss.: 11 April 2006
Revised: 18 October 2006 – Accepted: 20 October 2006 – Published: 16 April 2007

Abstract. Vertical profiles of CO_2 concentration were collected during an intensive summer campaign in a coastal complex-terrain region within the frame of the European Project RECAB (Regional Assessment and Modelling of the Carbon Balance in Europe). The region presents marked diurnal mesoscale circulation patterns. These circulations result in a specific coupling between atmospherically transported CO_2 and its surface fluxes. To understand the effects of this interaction on the spatial variability of the observed CO_2 concentrations, we applied a high-resolution transport simulation to an idealized model of land biotic fluxes. The regional Net Ecosystem Exchange fluxes were extrapolated for different land-use classes by using a set of eddy-covariance measurements. The atmospheric transport model is a Lagrangian particle dispersion model, driven by a simulation of the RAMS mesoscale model. Our simulations were able to successfully reproduce some of the processes controlling the mesoscale transport of CO_2. A semi-quantitative comparison between simulations and data allowed us to characterize how the coupling between mesoscale transport and surface fluxes produced CO_2 spatial gradients in the domain. Temporal averages in the simulated CO_2 field show a covariance between flux and transport consisting of: 1) horizontally, a CO_2 deficit over land, mirrored by a CO_2 excess over the sea and 2) vertically, the prevalence of a mean CO_2 depletion between 500 and 2000 m, and a permanent build-up of CO_2 in the lower levels.

Correspondence to: G. Pérez-Landa
(gorkapl@confluencia.biz)

1 Introduction

Uncertainties in carbon budgets can be reduced by assimilating atmospheric CO_2 concentration measurements into atmospheric-transport simulation models. This process, known as inverse modeling, is the usual basis for global studies (Ciais et al., 1995; Fan et al., 1998; Rayner et al., 1999; Bousquet et al., 2000; Gurney et al., 2002). However, using coarse-grid transport models introduces a number of limitations: (1) the model grid box does not represent a precise point-wise measurement, but rather an average concentration at a typical resolution of hundreds of kilometers; (2) these models do not realistically account for the heterogeneous nature of the surface fluxes; (3) they do not resolve small atmospheric scales that can be relevant in the transport; and (4) they may not resolve the covariance of mixed-layer height with CO_2 fluxes and the pertaining "rectification" gradients.

To overcome these problems, several studies have used regional transport models with a typical grid of 30–50 km (Chevillard et al., 2002; Lin et al., 2004). In general, mesoscale models of this type produce a better agreement with CO_2 concentration data at continental sites than do global models. Nevertheless, over complex terrain, or if the CO_2 fluxes are very heterogeneous within each grid cell, many important transport features cannot be resolved. This supports the use of even finer-scale mesoscale models that can be brought down to 1 km to better account for heterogeneous fluxes and transport and their interactions (Nicholls et al., 2003; Lu et al., 2005).

Published by Copernicus GmbH on behalf of the European Geosciences Union.

We use here a fine-scale mesoscale atmospheric transport model to simulate the time-varying CO_2 distribution over the complex terrain area of the Valencia basin in eastern Spain. The ecosystem's CO_2 fluxes are estimated with an idealized flux model. The model results are compared to CO_2 concentration measurements made during an intensive campaign to investigate the processes leading to CO_2 variability at various scales.

The study has four main objectives: (1) to test the use of CO_2 as a tracer of fine-scale transport processes over a complex terrain region, (2) to quantify diurnal coupling between mesoscale transport and CO_2 flux variability, (3) to estimate the contribution of regional CO_2 sources to the observed CO_2 concentration signals, and (4) to gain knowledge about how local processes are transmitted to the regional scale.

We begin by describing the CO_2-concentration and surface-flux measurements made during the campaign (Sect. 2). Then, in the context of the regional mesoscale dynamical processes (see also Pérez-Landa et al., 2007), we describe both the Lagrangian particle dispersion model used for transporting CO_2 under these dynamical fields and the idealized model of biotic and fossil CO_2 fluxes (Sect. 3). We make a qualitative comparison of modeled and observed CO_2 diurnal variability at local (Sect. 4) and regional scales (Sect. 5) in terms of the coupled daily cycle of mesoscale and biotic processes. Finally, we analyze the effects of these processes on the temporal averages of the simulated CO_2 distribution in the Valencia region (Sect. 6).

2 Observed fluxes and CO_2 concentrations during the campaign

The two-week experimental campaign took place near the city of Valencia in the summer of 2001, as part of the European project RECAB (see http://www.bgc-jena.mpg.de/public/carboeur/projects/rec.html). We made: (1) airborne CO_2 concentration measurements both on horizontal transects near the surface and on vertical profiles (at repeated intervals during the day), (2) airborne eddy-covariance CO_2 flux measurements on the horizontal transects and, (3) eddy-covariance flux tower measurements at two representative ecosystem sites. In addition, we collected supporting data to be used to interpret the CO_2 signals: airborne meteorological observations and fluxes of water vapor and energy. These datasets, together with the atmospheric circulation patterns, were described in the companion paper by G. Pérez-Landa et al. (2007, referred to as P06). We focus our analysis on 2 July, a day that was representative of mesoscale circulations development (see P06) and that also provided enough measured profiles to characterise the diurnal cycle of the processes.

2.1 Airborne CO_2 concentrations

The aircraft routes for the 2 July campaign are detailed in Fig. 1. In-situ CO_2 measurements were collected onboard a Sky Arrow aircraft by means of a LICOR 7500 open-path infrared analyzer operating at 50 Hz (Gioli et al., 2004). Twelve airborne CO_2 transects were made at either 25 m or 50 m above ground level, predominantly over rice-paddies (black line in Fig. 1). Vertical profiles of CO_2 were taken between 25 m and 800 m at 06:23, 07:40, 11:47 and 13:03 UTC over a rice paddy field at the northern edge of the horizontal transects, south of the city of Valencia (see Table 1 in P06). In addition, airborne flask samplings were carried out at five discrete heights between 100 and 1500 m at 07:43, 11:21 and 14:51 UTC by a second airplane flying above citrus orchards about 5 km west of the rice field site (Fig. 1). Subsequently, the flasks were analyzed at the Max Planck Institute for Biogeochemistry in Jena (Germany) for the CO_2, N_2O, and CH_4 mixing ratios and for the stable isotopes in CO_2 (Schumacher, 2005).

2.2 Airborne and ground-based eddy covariance fluxes

Airborne fluxes of CO_2 and H_2O were measured during each horizontal transect, using a 3 km space length and applying methods described in Gioli et al. (2004). Ground-based eddy covariance flux tower measurements are made at a pine forest called El Saler (SA) and at a rice paddy field (RI). Both sites are located in close proximity to where the vertical profiles were sampled (Fig. 1). The SA flux tower (15.5 m) has been operational since 1998, and measures a dense natural maquia canopy (1–2 m) with an overstorey dominated by Pinus halepensis trees (50 to 100 years old and approximately 12 m in height). Soil is sandy, well-drained and classified as arenosol calcareous (FAO, 1998). The rice paddy flux tower (2 m), over a rice canopy of about 60-cm in height, was set up only for the duration of the campaign. Soil is clay loam (upper horizon, 0–30 cm) and silty clay loam (deeper than 30 cm) and is classified as fluvisol calcareous (FAO, 1998). For eddy covariance measurements, wind velocity and temperature fluctuations were measured with a 3-D ultrasonic anemometer (model Windmasterpro, Gill Instruments Ltd., Lymington, UK), and H_2O and CO_2 fluctuations were measured with a closed-path infrared gas analyzer (IRGA; model LI-6262, Li-Cor Inc., Lincoln, USA). Data were collected at a 20 Hz sampling rate and 30-min fluxes were calculated using eddy-covariance software (Alteddy 1.2, Alterra Green WorldResearch, Wageningen, The Netherlands). The eddy system and data processing followed the standard Euroflux methodology (Aubinet et al., 2000). Supporting meteorological measurements were performed at SA and stored as 10-min averages. They include incoming photosynthetically active radiation (PAR) (LI-190SA Quantum sensor, Li-Cor Inc., Lincoln, USA) and air temperature (AT1 Thermistor, Delta-T Devices Ltd, Cambridge, UK).

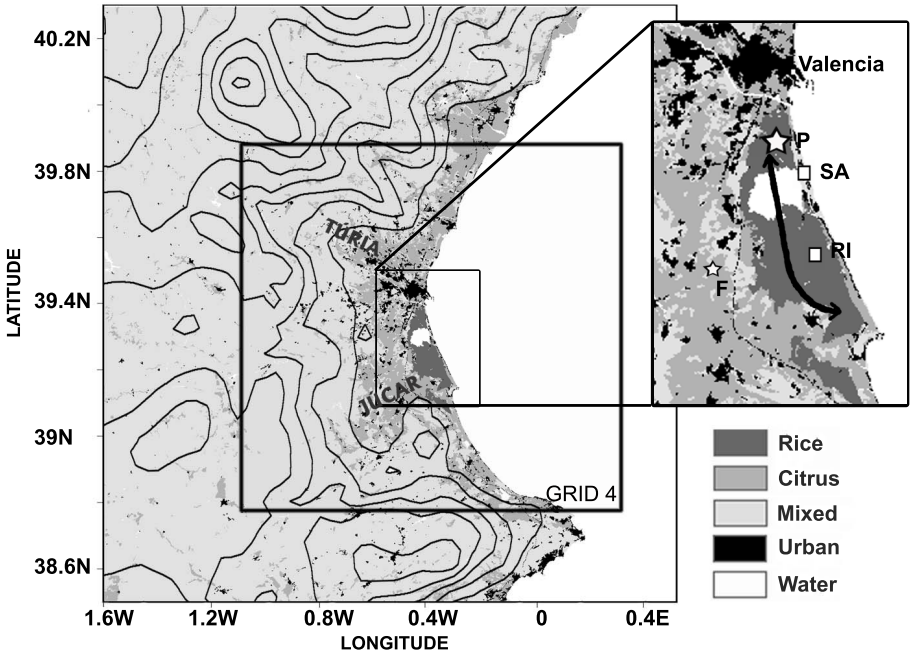

Fig. 1. Land cover types in the Valencia region (see legend). Contour lines show the orography every 200 m. The location of the smallest-domain for simulated meteorology using the RAMS mesoscale model is indicated by the black solid line (Grid 4). The campaign region is zoomed to show the location of the eddy-covariance flux towers (squares) at El Saler pine forest (SA) and over the rice paddies (RI), airborne horizontal transect (black arrow), vertical profile (big star, P), and flask air sampling (small star, F).

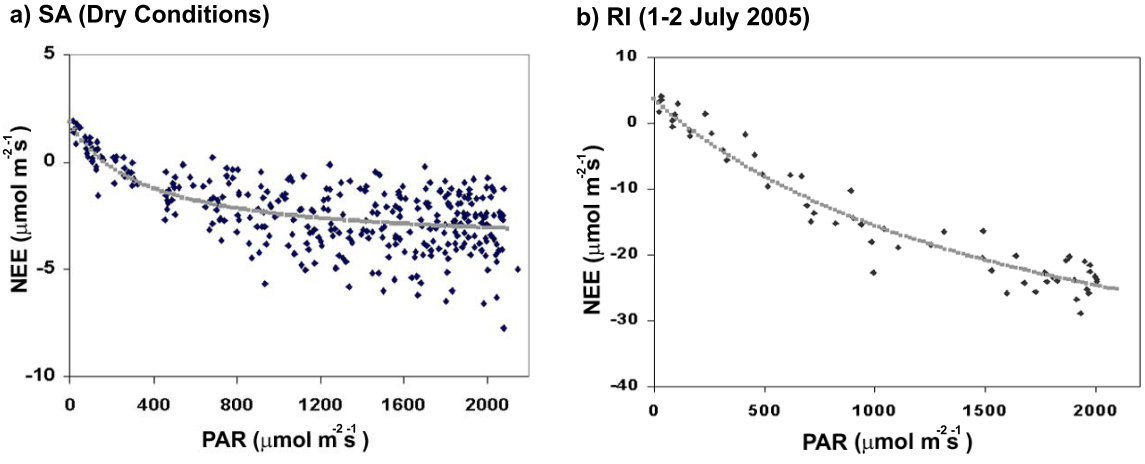

Fig. 2. Observed vegetation atmospheric CO_2 flux (NEE in μmol m^{-2} s^{-1}) as a function of solar radiation in the PAR domain (μmol m^{-2} s^{-1}): **(a)** El Saler (SA in Fig. 1) during the days selected for driest conditions between June and August 2001, **(b)** the Rice tower (RI in Fig. 1) during 1–2 July.

3 Models of CO_2 fluxes and transport

3.1 Atmospheric dynamical model

The transport of CO_2 is simulated using surface fluxes from an idealized spatial flux model (see Sect. 3.2) and the 3-D dynamical fields pre-calculated from the RAMS mesoscale model. The RAMS model is described in P06, and here we only recall the main model input data and results. The RAMS 4.3.0 non-hydrostatic model was nested three times with increasing horizontal grid spacing, going down to the campaign domain bounded by 1 W, 38.8 N and 0.4 E, 39.9 N (Fig. 1). Within the campaign domain, the model horizontal resolution is 1.5 km, and its vertical grid spacing increases

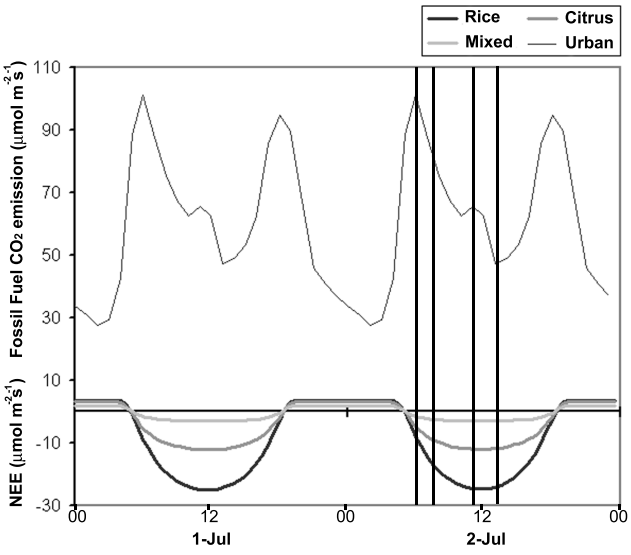

Fig. 3. CO_2 fluxes estimated according to the text, on 1 and 2 July for the different vegetation types and urban emissions (μmol m^{-2} s^{-1}). Solid vertical lines represent the times of the available profiles observed on 2 July.

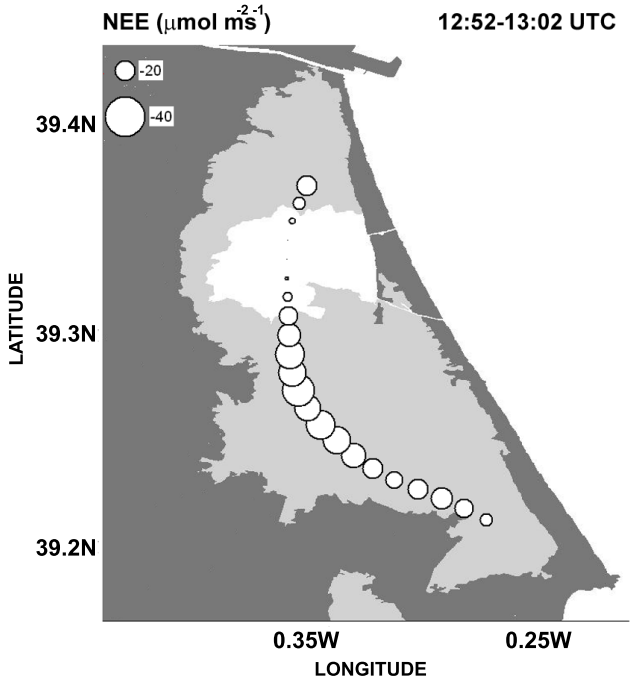

Fig. 4. Airborne CO_2 Fluxes at height of 25 m above the Rice paddies measured between 12:52 and 13:02 UTC. The size of each circle is the CO_2 Flux density in μmol m^{-2} s^{-1}.

gradually from 30 m to 1000 m, with the model top being 17 000 m. There are 15 levels in total below 1000 m. The model is forced at the lateral boundaries of its largest nesting domain by large-scale meteorological analyses (Caplan et al., 1997). Soil temperature and soil moisture are initialized from a two-month spin-up simulation. P06 found that the key dynamical mesoscale features reproduced by RAMS during the episode were: (1) a nocturnal drainage flow driven by terrain shape and gravity, (2) a morning sea-breeze development and inception of up-valley breezes, (3) an early-afternoon, "combined-breeze", where air parcels become sucked inland, uplifted on mountain slopes, and return seawards at altitudes lower than 3 km and, (4) a southward shift in the breeze flow during the late afternoon of 2 July.

3.2 Net Ecosystem Exchange (NEE)

We constructed a spatial NEE model based on simple land-use classes and point observations. In such an idealized model, NEE depends only on radiation in the photosynthetically active domain (PAR) and on land-use changes. We considered three dominant land-use types on the basis of the pan-European CORINE database at 50 m resolution (CEC, 1995): Rice, Citrus, and Mixed. Rice is an irrigated and highly productive crop and has a higher daytime-NEE uptake than other ecosystems. Rice paddies covering 15 000 ha of the model domain (5% of flat areas) are just under the aircraft profiles, and thus will influence strongly the CO_2 concentration signals there (see Sect. 4). The Citrus land-use class corresponds to the many orange tree plantations in the Valencia region, and are referred to as "Fruit trees and berry plantations" in the CORINE database. This is the dominant vegetation type in the coastal plains (68% of flat areas for an area of 269 000 ha). The Mixed land-use class groups "Complex cultivation patterns" (20%), "Coniferous forest" (20%), "Sclerophyllous vegetation" (35%) and "Transitional woodland-scrub"(17%), which all together cover 69% of the total domain, and 95% of the mountainous areas.

Our idealized NEE assumes a common set of parameters for each land-use type i, based on point flux tower measurements (see Table 1). The NEE equations are:

$$\text{If nighttime : NEE}=c_i \tag{1}$$

$$\text{If daytime : NEE}=c_i-\frac{a_i\times\text{PAR}}{(1-\text{PAR}/2000+a_i\times\text{PAR}/b_i)} \tag{2}$$

Where c_i is the average of the quality-checked nighttime NEE measurements (i.e. respiration). The parameters a_i and b_i are fitted by least-square method using quality-checked daytime NEE data. Equation (2) is a modified form (see Falge et al., 2001) of the Michaelis and Menten (1923) hyperbolic shape.

The Rice vegetation parameters are inferred from the eddy-covariance data of 1–2 July (Table 1). The modeled Rice NEE at mid-day shown in Fig. 3 is in good agreement with the independent airborne flux measurements shown in Fig. 4., a feature already pointed out by Gioli et al. (2004). Parameters for the Citrus land-use class could not

be determined during the campaign; instead, we used eddy-covariance fluxes measured on a nearby site in July 1995 (Seufert et al., 1997).

For the Mixed land-use class, we also lacked direct eddy-covariance data. Likely, the complex terrain effects and local differences in soil moisture availability and rooting depth will cause a large spatial variability in NEE. The SA Maquia forest is similar to the forests and shrublands that dominate the Mixed land-use class, but its greater proximity to the sea creates wetter conditions (due to the breeze regime) than over most of the inland forest regions. Therefore, to constrain the model parameters for Mixed land-use class, we selected the driest NEE episodes registered at the SA tower. We identified 12 days between mid-June and mid-August 2001, during which the mesoscale conditions consisted of dry and warm conditions in the absence of a sea breeze (with daily maximum air temperatures of $\approx$32.4$\pm$2.0°C and daily minimum air relative humidity of 30.3$\pm$3.9%, similar those encountered over the Mixed land-use class, as shown in Fig. 3 in P06). Under such an atmospheric water stress regime, the NEE in the SA forest at optimum PAR (Fig. 2) was on average 62% lower than the "normal" values (not shown). The NEE patterns were coarsely extrapolated to the whole domain using the land-use classes maps (see above) and PAR variations. The point-wise PAR measurements from the SA site were assumed to be representative of the whole domain under clear sky conditions (as was the case during the campaign). The resulting NEE temporal variations for each land-use type are illustrated in Fig. 3. This idealized NEE model represents real surface CO_2 fluxes with high uncertainties due to different sources of error: a) error associated to eddy covariance measurements, b) potential bias due to mismatch between flux measurements footprint and sources regions, c) spatial variability within source regions not accounted for. An independent analysis of NDVI patterns (see Appendix A) suggests that our coarse NEE extrapolation scheme captures well the higher NEE over rice than over citrus, but underestimates both the mean NEE and its spatial variability ($\pm$14% within small regions) over the Mixed land- use class.

3.3 Fossil fuel emissions

Urban areas cover 3% of the campaign domain and 7% of the flat area. The city of Valencia, with 0.8 M inhabitants (60% of the region) is a major CO_2 fossil fuel source. It is located just 10 km north of the vertical profiles. Detailed regional fossil fuel CO_2 emission inventories do not exist. Thus, we disaggregated the annual mean fossil fuel CO_2 emissions reported at the first spatial resolution for the year 1995 in the EDGAR 3.2 global inventory (Olivier et al., 2001) over the campaign domain and increased this by 22% in order to account for rising Spanish trends between 1995 and 2001 (Marland et al., 2003). All the fossil fuel CO_2 emissions in the EDGAR 3.2 grid cell are distributed in the city of Valencia (75.9 km^2), disregarding smaller cities and roads. This gives an emission rate of 4.76×10^9 gC day^{-1}, which corresponds to a flux of 62.7 gC m^{-2} day^{-1} in the city area. This value is much stronger that the mean daytime NEE uptake flux by vegetation of –3.73 gC m^{-2} day^{-1} for the whole domain (see Fig. 3). A mean diurnal cycle is assigned to the fossil fuel CO_2 emissions by using data from the Valencia-city air quality network. Car traffic is the dominant source of CO_2 in the city area. Since cars always emit CO together with CO_2, the diurnal shape of fossil CO_2 emissions could be estimated by using hourly CO measurements from three representative air quality stations located inside the city for every June and July over the period 1996–2001 (see data at http://www.cth.gva.es/cidam/emedio/atmosfera/index.htm). The resulting fossil fuel CO_2 emissions shown in Fig. 3 show two pronounced peaks at around 07:00 and 17:00 UTC, corresponding to road-traffic rush hours.

Table 1. Parameters of the NEE simulation model for Mixed, Rice and Citrus vegetation, as deduced from different eddy-covariance datasets (see text).

	Mixed	Citrus	Rice
c_i	1.86	3	3.6
b_i	0.01642	0.025	0.03005
a_i	4.91	15	28.21

3.4 Lagrangian particle dispersion model

We transport CO_2 using dynamical fields pre-calculated by RAMS and the HYbrid Particle And Concentration Transport (HYPACT) Lagrangian particle-transport model (Tremback et al., 1994; Walko et al., 2001). The HYPACT model was formerly applied to the Mediterranean region by Gangoiti et al. (2001, 2002) and by Kotroni et al. (1999) to study the regional transport of pollutants. It was also used to diagnose the vertical injection of aerosols in the Alps (de Wekker et al., 2004) and to assess the importance of meteorological scales in air pollution forecasting over a coastal complex terrain area on the east coast of Spain (Palau et al., 2005).

The HYPACT particle dispersion model has the same domain configuration and nesting capabilities as RAMS, allowing us to prescribe surface sources at the RAMS maximum resolution, with either continuous or sporadic releases of particle packets. The three wind and TKE turbulence-field components are extracted from the RAMS output every 10 min and used to drive the HYPACT model. In HYPACT, particle transport is calculated from interpolated RAMS fields every 30 s, starting 30 h before collection of the first vertical profile at 06:23 UTC on 2 July and continuing for 48 consecutive hours following emission. Particle transport and dispersion are computed within the three nested domains, allowing us

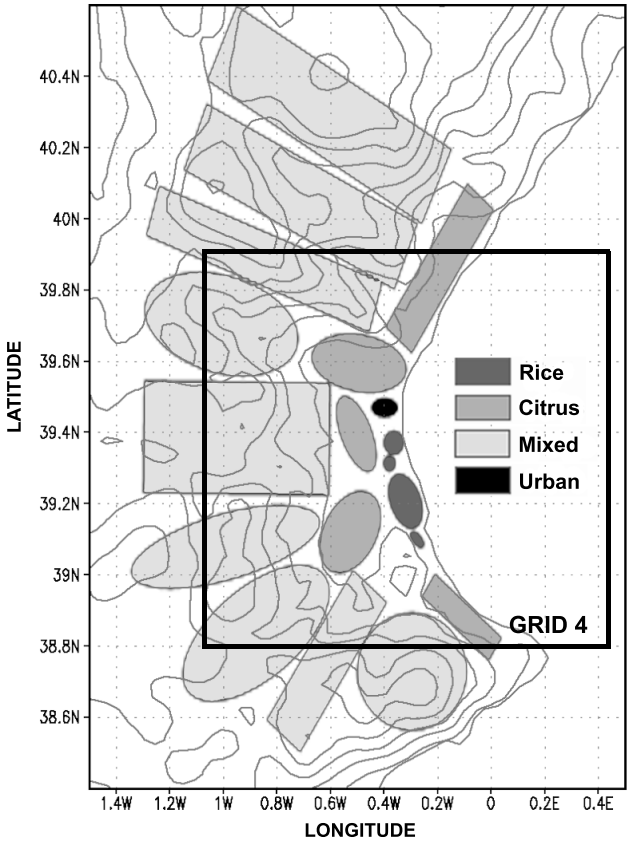

Fig. 5. Source regions considered in the particle dispersion model simulation. The colors represent the different land-uses indicated in the legend.

to simulate recirculations with veering winds. Note also that the Mixed land-use source regions are partly located outside the smaller model domain (Fig. 1) and are thus sending particles inside, which (partly) accounts for external regions contributing to CO_2 variations inside.

3.5 Source regions

Due to computing-power limitations, particles are not released from each RAMS grid cell but rather from a set of large source regions, as shown in Fig. 5. There are 18 different vegetated regions and one urban region. The contour of each region (Fig. 5) is chosen: (1) to be spatially coherent with the dominant vegetation types, (2) to follow the relevant terrain/flow information, and (3) to have a simple geometry. We chose, for instance, the five Citrus source regions with their symmetry axis parallel to the main valleys, so that their particles would form distinctly identifiable streams when drained by nocturnal winds. The source regions become smaller the nearer they are to the vertical profile site over the rice paddies (see Fig. 5). The simple geometry selected for the source regions leaves some gaps in area, shown as white areas in Fig. 5, with the result that the sum of the 19 regions covers only 78% of the inner domain. In order to avoid losing mass from these uncharted areas, we enhanced particle emissions from each source region by a scaling factor dependent on vegetation type, so as to match the total flux prescribed for that vegetation category.

3.6 From particles to concentration

Because of computing limitations, a particle packet could not be emitted from each grid cell at each time step in a region. So at each time step (20 s), a single particulate packet is emitted for the region at a randomly chosen grid cell. The temporal emission patterns change every 30 min, and follow the idealized NEE model. The CO_2 concentration pertaining to each regional source is obtained by dividing the number of particles found in a "detector" grid box by the corresponding number of moles of dry air simulated by RAMS. We keep track separately of concentration changes caused by sources emitting during each 30-min. interval. Each particle is assigned a mass of 300 gC so that at least 20 particles equate a concentration change of 1 ppm, the typical precision of airborne CO_2 measurements (see Appendix A1). Given the mass of each particle, for 19 regions multiplied by 96 separate concentration fields (30 min release intervals during a 48-h period), we calculated the dispersion of 29 million particles in total, which represents 14 days of CPU time on a 2 GHz local lab-top computer.

4 Observed and modeled CO_2 vertical profiles driven by mesoscale processes

Figures 6a–d shows the observed vertical profiles of CO_2 potential temperature, water vapor, and horizontal winds. We only briefly recall here from P06 what is important for understanding the CO_2 signals. A temperature inversion very near the ground is observed in the earliest profile at 06:23 UTC. The potential temperature profile indicates some vertical mixing below an inversion located at 200 m above the surface (Fig. 6c) in the 07:40 UTC profile. The sea breeze circulation starts soon afterwards, and the next two profiles at 1147 and 1303 show a mixed layer below 200 m (Fig. 6c). Above that height, stable conditions persist and are reinforced during the afternoon by the compensatory subsidence over the coast (discussed in P06). The solid circles in Fig. 6a represent the flask CO_2 measurements made above Citrus orchards 5 km west of the profiles over the Rice fields (Fig. 1). Despite the different location, the flask data show a gradual decrease in CO_2 concentrations in the lower levels during the course of the day, similar to the continuous profiles.

The model fails to reproduce the observed profiles quantitatively (Fig. 7). One reason for this is the very coarse nature of the NEE extrapolation scheme, which likely smoothes the spatial variations in fluxes and hence in concentrations.

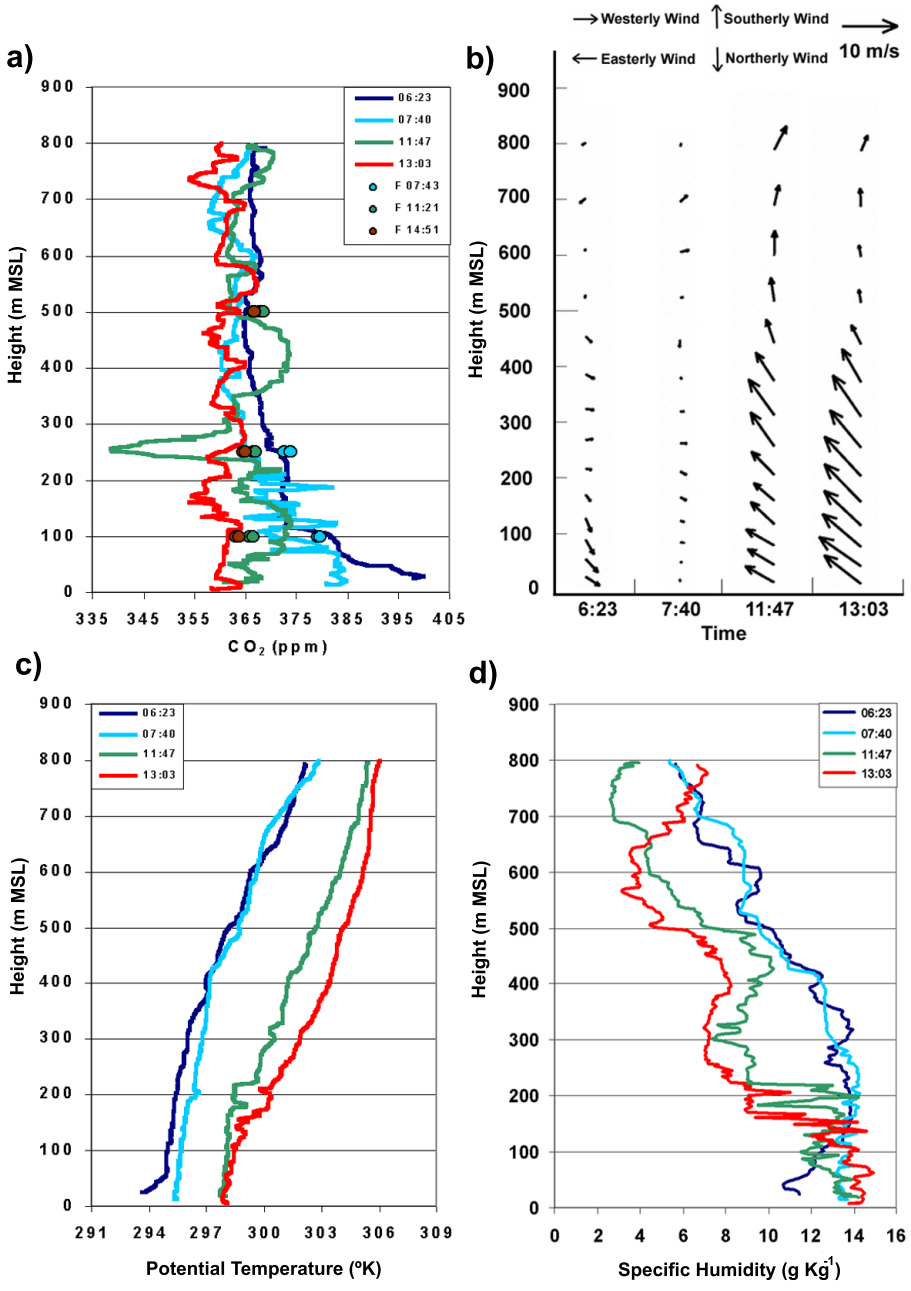

Fig. 6. Aircraft vertical profiles of **(a)** CO_2 concentration (ppm), **(b)** horizontal wind vector ($m\,s^{-1}$), **(c)** potential temperature (°K) and **(d)** water vapor ($g\,Kg^{-1}$) collected at successive intervals on 2 July of the campaign. Solid circles in (a) represent CO_2 measurements in flask air samples by another aircraft at a nearby location (see Fig. 1) at the corresponding times indicated in the legend.

The NDVI analysis carried out in Appendix A suggests that within each source region there is a spatial variability on the order of 14% of the regional mean NEE. This unmodeled variability probably causes the CO_2 fields to be too smooth. Also, errors in the NEE parameters create errors in the modeled CO_2. The sensitivity of the modeled profiles to NEE parameters (Appendix A2) suggests an error of 10 ppm in the morning (respiration errors) and 20 ppm in the afternoon (photosynthesis errors). There are also unmodeled transport contributions such as the contribution of large-scale advection, capable of advecting stable layers of pollutants in the region (Gangoiti et al. 2001). Finally, the applicability of available turbulence parameterizations under such conditions, or the limitations of the model in resolving layers of tenths of meters at feasible vertical resolutions, may also explain the differences with the data.

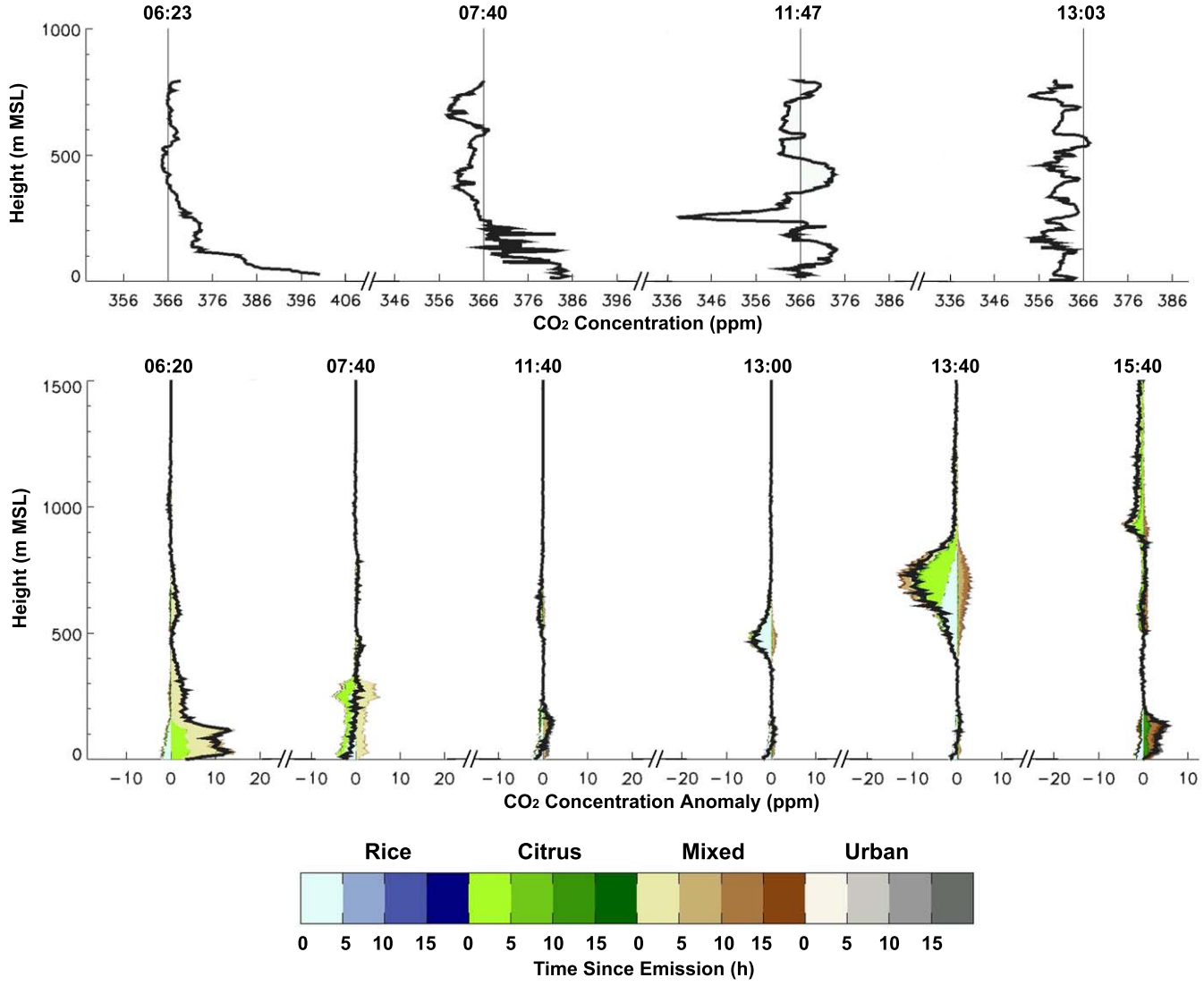

Fig. 7. Top: profiles of CO_2 (ppm) measured at P (Fig. 1) at different times on 2 July. Bottom: Simulated contribution to the simulated net CO_2 profile in P, at the corresponding time on 2 July, classified by origin and time since emission (shaded colors). Black solid line represents the net CO_2 profile obtained by adding negative and positive signals.

In Fig. 7, the comparison between modeled and observed profiles remains qualitative. It can be seen as an attempt to test the model's ability to reproduce the characteristic meteorological and biological processes. In this figure, the modeled CO_2 concentration is horizontally averaged over a 3-km radius around the aircraft profile site and is plotted vertically every 5 m. The contributions from different sources at different time intervals are also shown.

We have divided the one-day measurement period into three different consecutive stages in order to analyse the processes driving changes in the CO_2 vertical distribution. All times are expressed in UTC units.

4.1 Nocturnal regime

During nocturnal hours, respired CO_2 merges with stable drainage winds flowing towards the sea. The 06:23 profile shows a higher CO_2 concentration in the lowest 100 m than aloft. A pool of respired CO_2 is trapped inside the near-ground thermal inversion and advected towards the sea by drainage of katabatic winds (Figs. 6a–b). The observed near-surface CO_2 build-up amounts to 30 ppm; a back-of-envelope calculation in which 1.86 μmol m^{-2} of CO_2 (i.e., the Mixed land-use respired CO_2 flux in Table 1) is injected into a 100 m-thick surface layer for 8 consecutive nocturnal hours, gives a CO_2 accumulation of 15 ppm. In contrast to the data, the simulated vertical profile (see Figs. 6 and

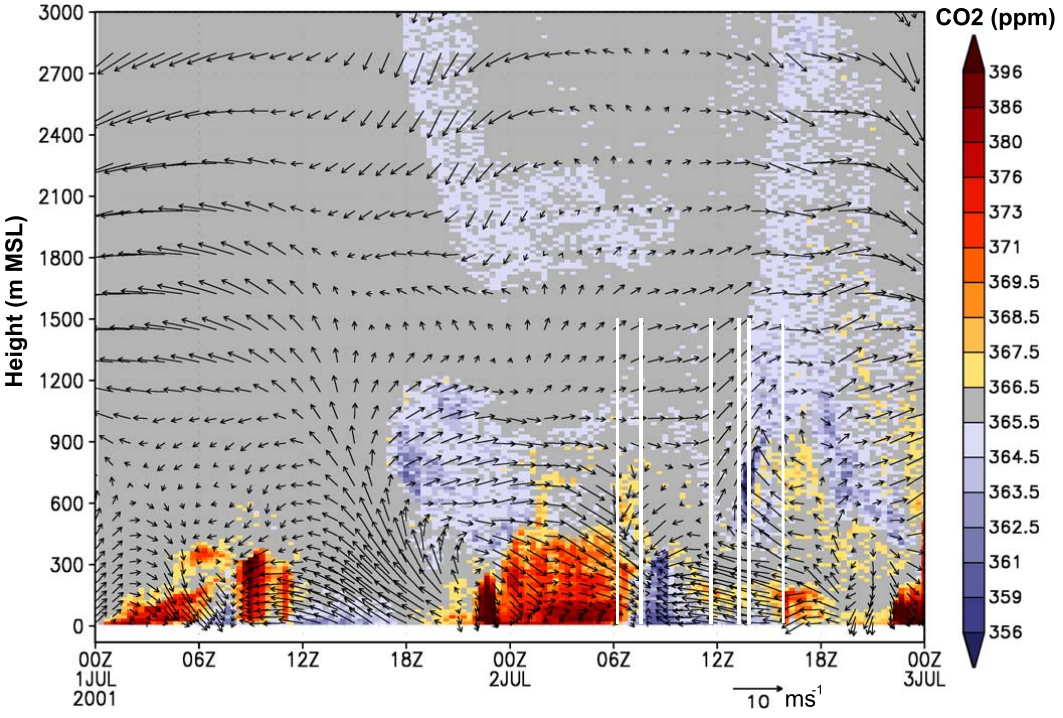

Fig. 8. Time series of the simulated profile of the lower 3 km of the atmosphere for wind ($m\,s^{-1}$) and CO_2 (ppm) at the place where continuous profiles were measured (see Fig. 1) on the 1 and 2 July. Wind arrows are plotted for every layer of the meteorological model and for every hour, while CO_2 concentrations are calculated every 20 m. Solid white lines represent the times of the vertical simulated profiles shown in Fig. 7. We added 366 ppm to the positive and negative simulated signal as an offset obtained from the average of the CO_2 values measured at the top of the four profiles considered in this study.

7) shows a near-surface CO_2 build-up of 10 ppm only. The CO_2 drainage pool is predominantly composed of molecules respired during the previous 5 h, coming from Mixed and Citrus land-use source regions. This could be due to an underestimation of the respiration from these classes, as is also indicated by the NDVI analysis (Fig. A2). Another factor that could explain this bias is the excess of simulated TKE during the stable conditions, since the shape of the modeled profile suggests more vertical mixing than observed. Moreover, the modeled drainage wind is too weak compared to the data (see P06), which could underestimate the fetch of the nocturnal drainage currents. Superimposed on these drainage effects, we simulate a local, small negative contribution of 1 ppm caused by the recent CO_2 uptake over Rice.

4.2 Transition between nocturnal and diurnal regimes

A transition between drainage winds and sea breeze inception occurs three hours after sunrise (at 07:40). This period is characterized by very low wind speeds (Fig. 6b). Photosynthesis and vertical mixing by turbulence act to decrease CO_2 in the lowermost part of the profile. Between 06:23 and 07:40, the data show a CO_2 decrease of 15 ppm, which would correspond exactly to the removal of CO_2 by the NEE of Rice vegetation (Table 1) from a 100 m thick surface layer. Just above the surface layer, there is some variability in the CO_2 profile, with occasionally higher values than at 06:23 (Fig. 6a), reflecting the uplifting of respired CO_2 in large convective eddies. In the model, the wind speed weakens at around 07:00, in good agreement with the observed transition to sea breeze flow (see also Fig. 8 and P06). During the transition, the modeled vertical mixing increases in the first 300 m of the air column (Fig. 7). At 07:40, we simulate a homogeneous CO_2 profile, containing opposite CO_2 contributions from nearby Rice and Citrus regions (Fig. 7). Unlike the model, the data still show an accumulation of CO_2 near the surface, because the initial nocturnal build-up was greater in the data than in the model at 06:30.

4.3 Diurnal regime

This stage is associated with the development of the breezes directed inland. At 11:47, the sea breeze was already developed (see winds in Fig. 6b). Photosynthetic uptake decreases CO_2 by 15 ppm from the earlier profile measured. The profile shows that between 200 m and 300 m there is a layer depleted of CO_2 by about 30 ppm (Fig. 6a). This layer is not apparent in the wind and H_2O profiles. Above this layer, the CO_2 builds up forming a "hump" of 15 ppm at a height of 400 m. By 13:03, the layer has disappeared, but variations of up to

5 ppm persist throughout the profile. Due to photosynthesis, a continuous decrease is observed in the CO_2, amounting to 5 ppm since the former profile at 11:47. The model does not agree quantitatively with the data, but it shows the formation of a depleted layer at 400 m. In the 11:40 profile, the source analysis suggests that no land-use class contributes to the profile (everything comes from the sea, where the flux is set at zero). Thus, the simulated CO_2 vertical distribution is homogeneous, except for a small Rice uptake signal (a negative 2 ppm) near the surface. Between 13:00 and 13:40, the modeled CO_2 profile shows a continuing decrease in CO_2 below 200 m, due to Rice uptake. The model produces a CO_2 layer depleted by 6 ppm at $\approx$500 m, which deepens and moves upwards between 13:00 and 13:40, and summing up to a total negative anomaly of –13 ppm (Fig. 7). It is encouraging to see that a high-resolution model can simulate the layering in the vertical CO_2 concentration distribution. By 13:00, the modeled layer contains the dominant signature of the recent Rice vegetation uptake to which the air mass was exposed. Later on, at 13:40, it receives additional contributions from the uptake over Citrus and Mixed land-use (Fig. 7). Interestingly, we diagnose a positive CO_2 contribution from the Mixed regions to the modeled layer. This positive CO_2 anomaly reflects the fact that 50% of the sources were active during the previous 5–10 h, besides those active 10–15 h earlier, that is, the respiration from the former night. The last profile simulated at 15:40 is influenced near the ground by Rice vegetation uptake and by old ($>$15 h) Citrus, Mixed and Urban sources. Above 900 m, there is a negative variation in the simulated CO_2 profile of –5 ppm, reflecting the action of Citrus and Mixed vegetation sinks that were active during the previous 5 h.

5 Basin-scale changes in CO_2 distribution driven by mesoscale processes

We now use the spatial and temporal coverage of the model output to explain CO_2 variations in the Valencia basin. The time-varying vertical distribution of the $CO_2$is shown in Fig. 8. Figure 9 shows the CO_2 distribution near the surface (0–30 m). A constant offset value of 366 ppm is added to simulated time-varying CO_2 concentration anomalies. This offset is chosen to be equal to the average CO_2 value measured at the top of the four aircraft profiles. At night the land drainage flows with elevated CO_2 values (up to 376 ppm) penetrate over the sea. In Fig. 9a, the maximum simulated values of CO_2 at 06:00 are located downwind of Valencia city. The city plume of fossil fuel CO_2 adds to the convergence of respired CO_2 streams channeled by the Xucar and Turia valleys to produce a "tongue" of CO_2-enriched air that extends more than 100 km away from the coast. At 06:00, the first effects of photosynthetic uptake appear over the sunny slopes of the mountains outside the valley flows. This produces lower near-surface CO_2 values (Fig. 9a).

At 08:00, during the transition regime, solar heating of the eastern slopes facilitates the development of local valley breezes. However, close to the coast and offshore, the CO_2 drainage pool formed during the night is still present (Fig. 9b). The horizontal wind convergence lines (Fig. 9b) at 08:00 indicate that vertical injection has started to occur locally. The flow shows a very complex circulation in which the scales of the processes are related to each valley's size and shape. Note also that there is a wind divergence from the center of each valley. Photosynthetic uptake has the effect of strongly decreasing CO_2 concentrations over land at 08:00 as compared to the previous 06:00 time interval. Given the shallow mixed layer height at this time, CO_2 near the surface drops abruptly from its highest to its lowest values of the day within only two hours (compare Figs. 9a and b). A generalized wind reversal from seaward to landward (Fig. 8), precludes the advection of this CO_2 uptake signal towards the sea. Thus, offshore elevated CO_2 concentrations are preserved in a stable "drainage lake" containing CO_2 respired from the former night.

Later in the morning, at 11:00, the sea and valley breezes begin to merge into a "combined breeze" (Fig. 9c). The combined-breeze circulation extends from over the sea where the winds diverge, up to the coastal mountain ridge parallel to the coast where the winds converge (see P06). In the northern part of Valencia, the convergence line is situated more remotely from the coast and lies outside the domain of the figure (but was still apparent from the simulation in the next coarser nesting domain). The "drainage lake" formed during the night becomes diluted and is swept back inland by sea-to-land breezes, producing a CO_2 maximum in the Southeast of the domain (Fig. 9c). Further inland, CO_2 is decreased by photosynthesis, with local minima over rice-paddy and citrus. The fossil CO_2 plume from the city is advected inland and channeled upward onto the Turia valley (Fig. 9c).

At 15:00 in the afternoon, the winds veer to the SE over the sea and the pattern of the convergence lines looks quite different from the one at 11:00, although the breeze persists (Fig. 9d). The high CO_2 concentration values from the remnants of the "drainage lake" are transported northerly across the campaign domain (compare Fig. 9c to Fig. 9e). Together with a gradual decrease in photosynthesis after noon, the passage of this CO_2 maximum explains why CO_2 remains 1.5 ppm higher near the coast than inland.

In the evening, the wind direction remains from the Southeast over the sea, but diverges over land and shifts to the Northeast in the southern part of the domain (Fig. 9e). Such a flow transition displaces the position of the mountain convergence lines, which re-organize as two "brackets" perpendicular to the coast (Fig. 9e). In the northern part of the domain, the fossil fuel CO_2 plume continues to accumulate in the Turia valley, with concentrations reaching above 373 ppm downwind from the city. Note also that 18:00 represents the local rush-hour traffic, which adds to the elevated plume concentration.

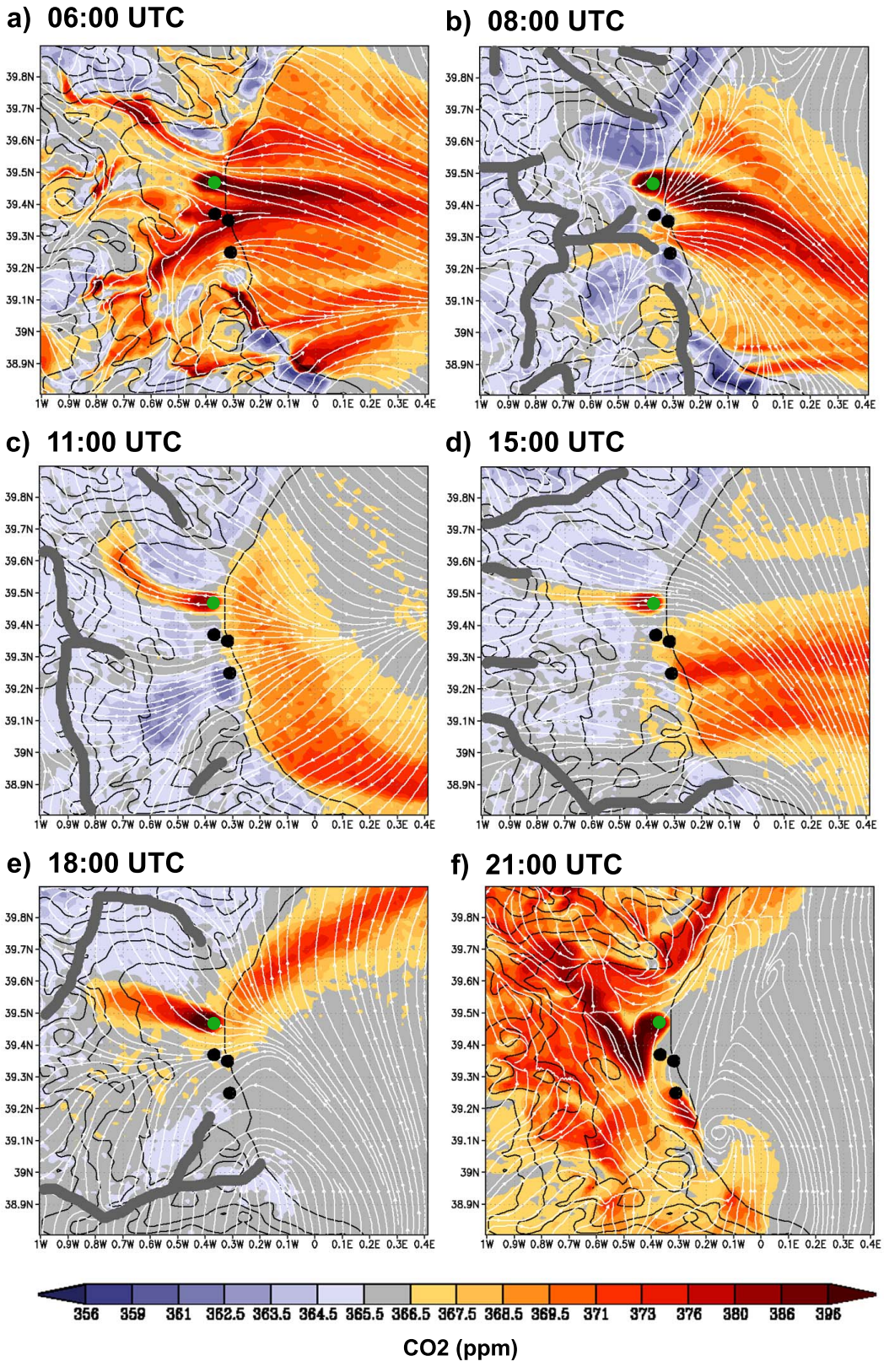

Fig. 9. Horizontal streamlines (white) and net CO_2 simulations (shaded colours) for the first level of the model at: **(a)** 06:00, **(b)** 08:00, **(c)** 11:00, **(d)** 15:00, **(e)** 18:00, **(f)** 21:00 UTC on 2 July. Solid dark grey lines represent convergence lines of the simulated horizontal wind.

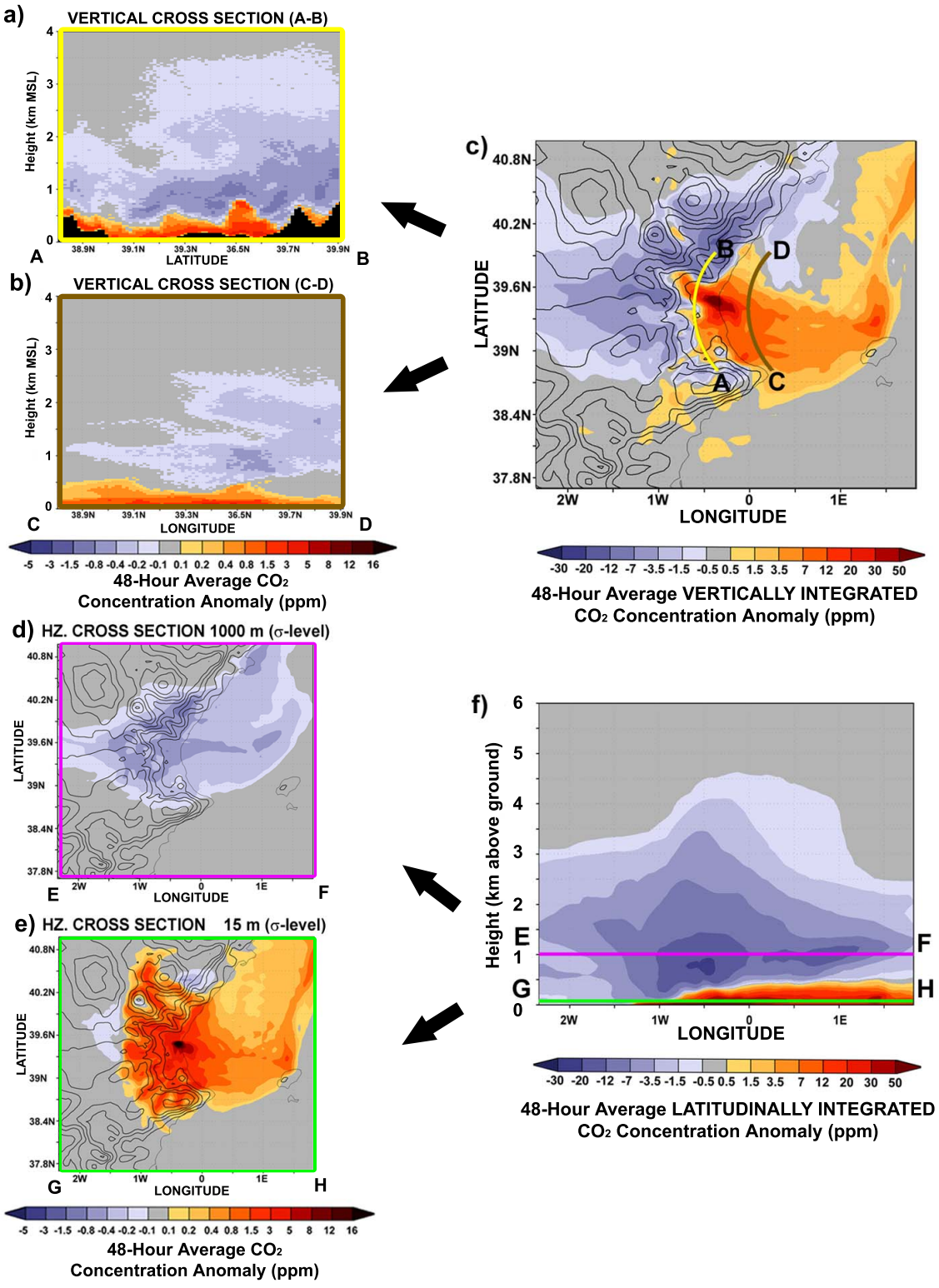

Fig. 10. The 48-h average simulated CO_2: **(a)** in the lower 4 km of the atmosphere following the inland cross-section A–B (yellow),**(b)** in the lower 4 km of the atmosphere following the sea cross-section C−D (brown), **(c)** vertically integrated in the whole regional domain, **(d)** at the 1000 m height sigma level (pink), **(e)** at the 15 m height sigma level (green) and **(f)** latitudinally integrated in the lower 6 km of the regional domain.

Finally at 21:00 (Fig. 9f), the nocturnal stage of the mesoscale circulation cycle begins again. The air cools sufficiently and starts forming katabatic drainage winds. The simulated CO_2 rises at all points near the surface up to values greater than 367 ppm, an increase driven by ecosystem respiration.

6 Spatial gradients in time-averaged CO_2 due to mesoscale processes

In this section, we investigate how the coupling between the periodic mesoscale circulation in the Valencia basin and the CO_2 surface fluxes generates gradients in the temporally averaged CO_2 distribution during the 48-h period. The time-averaged CO_2 concentration anomaly is noted as $<CO_2>$. Two modeled vertical cross-sections of $<CO_2>$ are shown in Figs. 10a–b. Both cross-sections are parallel to the coast and perpendicular to the main wind flow direction. One section is located 20 km offshore (Fig. 10b) and the other 20 km inland (Fig. 10a), to characterize the horizontal and vertical gradients.

The cross-section over land in Fig. 10a shows a vertical rectification gradient. The respiration and fossil fuel emission of CO_2 during the nocturnal regime, when stable conditions prevail, determines higher mean CO_2 concentration values in the lowermost 200 m. CO_2 assimilation by plants produces a broad $<CO_2>$ depletion aloft, between approximately 500 m and 2000 m (Fig. 10a). This $<CO_2>$ minimum reflects the transport of photosynthesis-exposed air parcels that: (1) can be injected at different distances from the coast and heights above the ground and (2) are sunk by the effect of compensatory subsidence while returning aloft towards the sea. When the convergence lines are consolidated along the ridges of the coastal mountain ranges, the injection occurs higher, which explains the depletion of $<CO_2>$ in the northern sector above 3000 m. The only exception to the generalized depletion in $<CO_2>$ observed above 500 m is the positive signal located up-valley of Valencia city. The city, emitter of fossil fuel CO_2, is the only source of positive signal active during the diurnal regime and is also exposed to the aforementioned mesoscale processes, whose effects create the increase in $<CO_2>$ inland at the lee of the city. In our study area, the 3-D character of the flow driven by mesoscale circulations explains why the $<CO_2>$ minimum compensating for the $<CO_2>$ maximum near the ground is modeled at much higher altitudes ($\approx$1000 m) than in "classic" diurnal rectifier simulations over flat terrain ($\approx$400 m) involving vertical dilution of photosynthesis by convective mixing (Denning, 1994; Denning et al., 1996). The specific role of breeze circulations in the vertical profile of $<CO_2>$ can also be seen by comparing the relatively modest daytime mixed layer height in Fig. 8 with the higher altitude of the mean CO_2 minimum in Fig. 10a.

Combined with this vertical rectification, there is also a horizontal covariance between flux and transport. The cross-section of $<CO_2>$ over the sea in Fig. 10b shows that positive signal concentration predominates in the lower levels and that there are two regions aloft where the depletion of $<CO_2>$ is present. This horizontal pattern is related to the features shown on the inland vertical cross-section, although some differences can be observed. The smoother horizontal signals are a consequence of the longer distance to the sources, and the altitudes where $<CO_2>$ depletion is observed are lower due to the greater subsidence over the sea. These location-dependent differences become more evident when analyzing the simulated $<CO_2>$ integrated in the vertical and horizontal direction in Figs. 10c and f. We observe in Fig. 10c that there is a $<CO_2>$ deficit over land, coupled with a $<CO_2>$ excess over the sea. The mean excess over the sea is created by the nocturnal drainage of respired CO_2. On the next day, it stagnates over the sea and becomes partially re-entrained back over land (Figs. 10e and 9). Most of this excess $<CO_2>$ is confined near the sea surface and over the coastal plains. Figure 10d shows the $<CO_2>$ minimum at the 1000 m height, corresponding to photosynthesis-exposed air parcels injected into the return flow during breeze development and horizontally stratified over the sea by compensatory subsidence.

The formation of such horizontal and vertical gradients in the mean CO_2 can be expected in many other coastal areas with similar mesoscale circulation features. For instance, the Western Mediterranean Basin is surrounded by mountain ranges which could all generate similar mesoscale CO_2 transport patterns. Extrapolating from our analysis, both a strong negative vertical gradient in $<CO_2>$ with increasing altitude and a large horizontal gradient in $<CO_2>$ with higher values over the sea and lower values inland could be expected as a result of the combined mesoscale effects at the WMB scale. This is very different from what a global model would simulate and, if proved to be widespread, such mesoscale effects should be considered at any station meant to measure "background" regional air.

If in the future we seek to map the effect of local fluxes from CO_2 concentration measurements, analysis of the spatial distribution of $<CO_2>$ in Fig. 10 suggests that a sampling strategy for inverting the regional carbon fluxes of the Valencia basin must consider taking vertical profiles of CO_2 from the ground to heights that can reach 3500 m during the afternoon. The high variability of the CO_2 vertical distribution in the lower 1500 m (Fig. 10) suggests that the sampling density should be high both spatially and temporally. One could then take vertical profiles simultaneously over the sea and at different locations inland to capture photosynthesis, and to use the drainage winds at night as a "laboratory assistant" to quantify regional respiration fluxes.

7 Summary and conclusions

Vertical profiles of CO_2 concentration were collected during an intensive campaign in the Valencia region, on the western Mediterranean coast. The marked diurnal cycle of the flow due to the development of mesoscale circulations, analyzed in P06, determines the CO_2 variations. We set up a 3-D Lagrangian particle dispersion model, driven by meteorology calculated from RAMS (P06). The regional distribution of NEE is coarsely extrapolated using a set of eddy-covariance measurements. The simulated CO_2 concentration field is compared with observed vertical profiles to study the transport processes. Because of limitations in the prescribed NEE, contributions from long-range transport and biases in modeled meteorology (see P06), our simulation could not match the observed profiles quantitatively. Despite such caveats and limitations, our CO2 transport simulation could successfully reproduce some of the important processes that control the mesoscale transport of CO_2. These processes are:

1) The nocturnal drainage circulation, which advects a shallow layer with high CO_2 values (from respiration) just above the sea to distances of up to 100 km away from the coast,

2) The diurnal transport of CO_2 by the breeze circulations which creates low CO_2 concentrations, due to air mass exposure to vegetation uptake in a relatively shallow mixed layer capped by subsidence,

3) The presence of lower CO_2 concentrations in airmasses that were injected along the convergence lines into the return circulation branch,

4) The evidence that compensatory subsidence limits the vertical dilution of the NEE daytime uptake of CO_2 by mixing and permits the formation of airmasses with a strong CO_2 deficit in the atmosphere. Such subsidence also increases the stability of the atmosphere above the mixed-layer top and contributes to maintain these strong CO_2 signals aloft,

5) The generation of a regional maximum and minimum in $<CO_2>$, with a negative vertical $<CO_2>$ gradient upwards and a negative horizontal $<CO_2>$ gradient seawards, showing a covariance between fluxes and transport. Vertically, the depletion in $<CO_2>$ prevails between 500 and 2000 m, while in the lower levels a permanent build-up of $<CO_2>$ persists.

These processes, identified here only for only one brief episode, may be frequently encountered in the Mediterranean atmosphere. In general, during the warm season, we expect the flow to show a marked 3-dimensional character and be highly sheared and in continuous transition between the different stages of the diurnal cycle that generates recirculation effects. This cycle could cause airmasses with different histories, different CO_2 signals and high temporal variability to be included in a given vertical profile. The mesoscale processes we have studied during a short campaign prevail in the Valencia region every year from April to September and should be taken into account in any future study aiming to explain the variability of CO_2 during the course of a year.

Studies on air pollution in the Western Mediterranean Basin have shown that similar mesoscale circulations are present in many of the regions with coastal mountains, where interaction at different scales generates a self-organization of the flow at basin level (Millan et al., 1997; Gangoiti et al., 2001). If this simulated distribution of the minimum and maximum atmospheric CO_2 concentration linked to mesoscale processes in the Valencia region is boldly extrapolated to the rest of the Western Mediterranean coastal regions, a large scale of horizontal and vertical gradients could occur around the whole basin. This hypothesis could be tested by combining mesoscale model approaches, using more realistic estimations of NEE, with vertical CO_2 profiles collected simultaneously over the sea and inland.

Appendix A

Analysis of uncertainties in the different components of the measuring/modeling systems

A1 Uncertainties in the vertical CO_2 and H_2O measurements

In the vertical profiles, CO_2 and H_2O number densities were measured with an open-path IRGA, and then mole fractions were computed using the temperature and static pressure measured by the Mobile Flux Platform. Errors in mole fraction computations can arise from errors associated with both static pressure and temperature measurements, as well as from errors related to the different positions of the static pressure measurement point and the IRGA optical path.

Static pressure Ps is measured by means of a pneumatic average of four points located at 41.8 deg on the MFP sphere. Errors in Ps can arise from sensor errors and from probe design, and a detailed error analysis can be found in Crawford and Dobosy (1992) along with results with an error of less than 1% q within normal operating range, where q is the dynamic pressure, around 0.1 kPa at SkyArrow flight speed. An uncertainty of less than 0.15°K in absolute temperature measurement using the MFP equipment has also been reported by Crawford and Dobosy (1992). The IRGA optical path has a real pressure that is different from the pressure measured on the sphere because of the aerodynamic effects that occur on the IRGA body. Such a difference is a function of aircraft air speed and attitude angles, and we estimate (from computational fluid dynamics, data not shown) that an error of

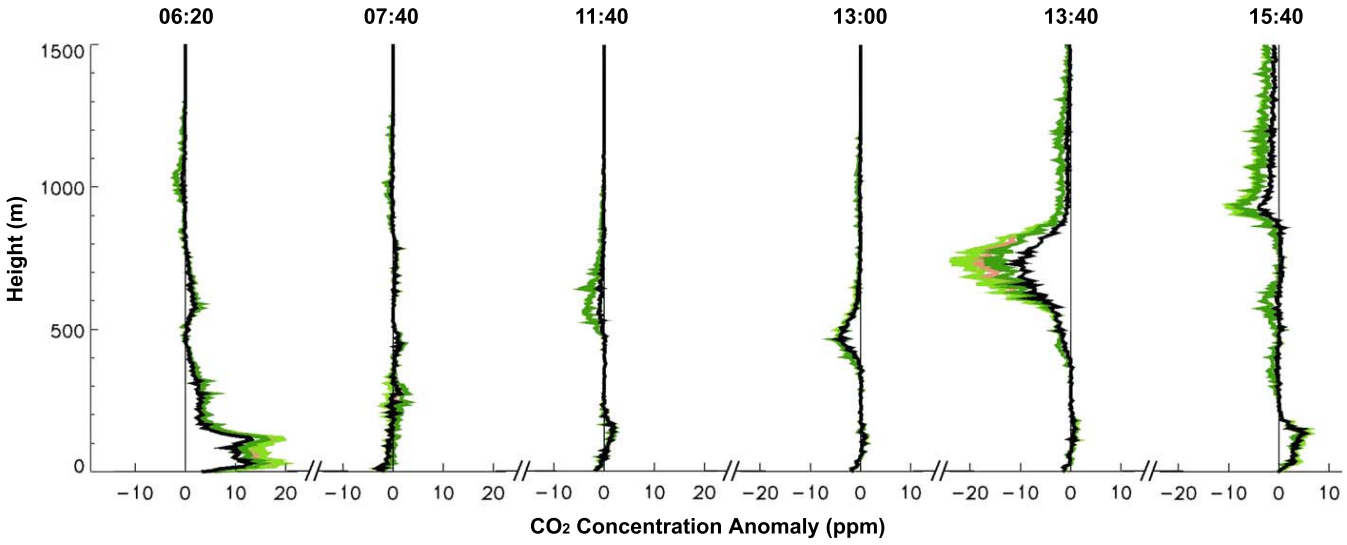

Fig. A1. Sensitivity test of the simulated vertical CO_2 profiles to the NEE estimation. R0, C0 and M0 represent the Rice, Citrus and Mixed land uses, with the parameters obtained in Sect. 3.2 and M+, C+ and C− being defined according to the Appendix. R0C0M0 (black) represents the control case. The three tests performed are: R0C0M+ (brown), R0C+M+ (green) and R0C−M+ (dark green).

less than 0.7 KPa is associated with pressure measurements on the MFP sphere.

By combining such multiple error sources into the absolute concentration computation, an accuracy of ± 3 ppm is obtained for the experimental data.

A2 Estimation of NEE

To test the approach used in this study to estimate vegetation fluxes, we performed some sensitivity tests to check the consistency of our results with respect to the simulated CO_2 vertical variations described in Sect. 4. The selection of the dry-condition days in SA to obtain the parameters in Eq. (1) was considered adequate for representing the vegetation activity under inland conditions during the campaign (Sect. 3.2). In case M+ (see Table A1) we estimated the SA parameters during the two-week campaign under normal conditions (moderate temperature and humidity). Thus, we were able to establish a high-level vegetation activity that helped us to estimate the influence of error in the flux estimation of this land use. Case C+ (C−) in Table A1 aims to represent the high (low) level activity of the Citrus orchards, where the parameters are obtained by increasing (decreasing) the CO_2 fluxes in the fitting of Eq. (1) by 50%. We consider that the parameters estimated from the eddy-covariance tower data at the rice field (Table 1) can be regarded as representative of the totality of rice fields because all the crops are located in a region under similar conditions. This was confirmed by the aircraft horizontal transects (Fig. 4).

We tested 3 cases by combining M0 and C0 (parameters according to Sect. 3.2 in both cases), M+, C+ and C− to obtain the maximum variation in the flux estimation. Figure A1 shows that the three cases present vertical distributions similar to the control case. Although there is a quantitative change in the values of the layers, the main conclusions of this study regarding the vertical distribution of CO_2 in a coastal complex terrain region are not affected.

Table A1. Parameters of the NEE simulation model obtained for Mixed under normal (not dry) conditions (M+) and estimated to test the sensitivity of the study to an increase of 50% (C+) and a decrease of 50% (C−) in the activity of the Citrus landuse considered.

	M+	C+	C−
c_i	2.86	4.5	1.5
b_i	0.00246	0.0375	0.0125
a_i	12.83	22.5	7.5

A3 Estimation of the spatial distribution of sources

To check whether the source distribution established in the CO_2-transport simulation with HYPACT in Sect. 3.5 permitted a realistic distribution of the vegetation activity in the whole region, we compared it with the NDVI (Normalized Difference Vegetation Index) obtained from satellite data (SPOT 4 VEGETATION data, available at http://free.vgt.vito.be, CNES copyright) during the 10 days composite period centered on 1 July 2001 (Fig. A2). We calculated the average and the standard deviation of NDVI in each

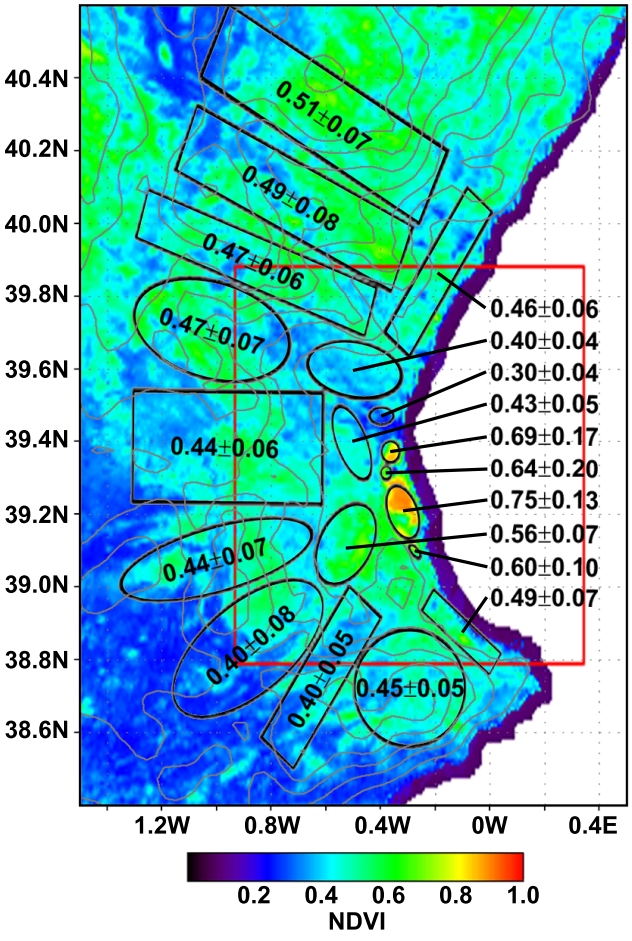

Fig. A2. NDVI estimated from satellite. Colours represent values for every pixel of 1 km^2 during the 10 days composite period centered in 1 July 2001. Numbers represent the average and standard deviation of the values in each of the 19 emission sources defined in the transport model, indicated by black solid line.

of the 19 sources configured in Sect. 3.5. It was clear that the sources that represent rice fields present the highest values of NDVI (all higher than 0.6), while the lowest values correspond to the City (0.30). The spatial variability of NDVI is around 14% of the corresponding mean for each of the sources defined as Mixed land-use. This can cause important limitations in the simulations of the contributions of Mixed sources to the simulated CO_2. Regarding the mean values of each source, Mixed and Citrus categories may be inconsistent with our study for the sources located to the north of 39.6 latitude. South of this latitude, our estimation regarding vegetation activity seems to show more coherence with the differences in averaged NDVI for Citrus and Mixed sources. This limitation has a moderate impact on our simulation of the CO_2 profiles, as the analysis of the source areas that contribute to the concentration signals showed that 87% of the simulated CO_2 concentrations came from sources located south of the 39.6 latitude.

A4 Uncertainty in the modeled transport

Our model approach is based on the results of the RAMS meteorological simulations described in P06. This companion paper evaluates the skills of the model, in simulating the different flow regimes during the selected case. The statistical comparison between the observed and simulated wind in seven meteorological ground stations during the 1 and 2 July showed an Index of Agreement of 0.79, a RMSE of 1.54 $m\,s^{-1}$, and a VWD of 2.18 $m\,s^{-1}$ (see Table 2 in P06), which are very good values if compared them with recent results using similar modelling strategies (or tools) in different air quality studies (as referred to in P06; e.g., Seaman and Michelson, 2000; Hanna and Yang, 2001; Zhong and Fast, 2003). It is difficult to quantify how the uncertainty in modeling meteorology will affect the transport simulation of any tracer. In a nearby region under similar meteorological conditions, Palau et al. (2005) showed similar statistical skills using RAMS to simulate the dispersion from a coastal power plant by means of HYPACT. In their study, the availability of remote sensing measurements (COSPEC) of the power plant plume aloft, permitted the direct evaluation of the dispersion model simulation of the diurnal evolution of the plume integral advection. Figures 5 and 6 of the referred study showed that the coupling of both models could capture the plume veering generated by the diurnal cycle, although some deviations in the dispersion were reported. Given the similarities between this study and ours with respect to conditions and uncertainty it is logical to expect biases in the dispersion, which could have an impact on the value of the simulated concentration. It is also reasonable to expect that our modeling scheme will likewise be capable of simulating the diurnal transport cycle for the different CO_2 sources configured.

Acknowledgements. This work has been partially supported by the projects RECAB (EVK2-CT-1999-00034) and CARBOEUROPE-IP (GOCE-CT-2003-505572), funded by the European Commission. The authors wish to thank all those who worked hard to collect the data in the field. We are grateful to D. Sotil for his support with the graphics. Also thanks to J. A. Alloza and J. V. Chordá for reclassifying CORINE and PELCOM physiography data into RAMS land use categories. J. Scheiding's corrections of the English text are appreciated. NCEP and ECMWF are acknowledged for providing meteorological analysis and reanalysis data. The CEAM foundation is supported by the Generalitat Valenciana and BANCAIXA.

Edited by: W. E. Asher

References

Aubinet, M., Grelle, A., Ibrom, A., Rannik, U., Moncrieff, J., Foken, T., Kowalski, A. S., Martin, P. H., Berbigier, P., Bernhofer, C., Clement, R., Elbers, J., Granier, A., Grunwald, T., Morgenstern, K., Pilegaard, K., Rebmann, C., Snijders, W., Valentini, R., and Vesala, T.: Estimates of the annual net carbon and water

exchange of European forests: the EUROFLUX methodology, Adv. Ecol. Res., 30, 113–175, 2000.

Bousquet, P., Peylin, P., Ciais, P., LeQuere, C., Friedlingstein, P., and Tans, P.: Regional Changes in Carbon Dioxide Fluxes of Land and Oceans Since 1980, Science, 290, 1342–1346, 2000.

Caplan, P., Derber, J., Gemmill, W., Hong, S. Y., Pan, H. L., and Parish, D.: Changes to the NCEP operational medium-range forecast model analysis/forecast system, Wea. Forecasting, 12, 581–594, 1997.

CEC (Commission of the European Communities): CORINE Land cover, Guide Technique, Brussels, available online: http://reports.eea.eu.int/COR0-landcover/en, 1995.

Chevillard, A., Karstens, U., Ciais, P., Lafont, S., and Heimann, M.: Simulation of atmospheric CO_2 over Europe and Siberia using the regional scale model REMO, Tellus, 54B, 872–894, 2002.

Ciais, P., Tans, P. P., Trolier, M., White, J. W. C., and Francey, R. J.: A large northern hemisphere terrestrial CO_2 sink indicated by the 13C/12C ratio of atmospheric CO_2, Science, 269, 1098–1102, 1995.

Crawford, T. L. and Dobosy, R. J.: A sensitive fast response probe to measure turbulence and heat flux from any airplane. Bound.-Layer Meteorol., 59, 257–278, 1992.

De Wekker, S. F. J., Steyn, D. G., and Nyeki, S.: A comparison of aerosol layer- and convective boundary layer structure over a mountain range during STAAARTE '97, Bound.-Layer Meteorol., 113, 249–271, 2004.

Denning, A. S., Collatz, J. G., Zhang, C., Randall, D. A., Berry, J. A., Sellers, P. J., Colello, G. D., and Dazlich, D. A.: Simulations of terrestrial carbon metabolism and atmospheric CO_2 in a general circulation model, Part 1: Surface carbon fluxes, Tellus, 48B, 521–542, 1996.

Denning, S.: Investigations of the transport, sources and sinks of atmospheric CO_2 using a general circulation model, PhD Thesis, Colorado State University, 1994.

Falge, E., Baldocchi, D. D., Olson, R. J., Anthoni, P., Aubinet, M., Bernhofer, C., Burba, G., Ceulemans, R., Dolman, H., Granier, A., Gross, P., Grünwald, T., Hollinger, D., Jensen, N. O., Katul, G., Keronen, P., Kowalski, A. S., Ta Lai, C., Law, B. E., Meyers, T., Moncrieff, J., Moors, E., Munger, J. W., Pilegaard, K., Rannik, U., Rebmann, C., Suyker, A., Tenhunen, J., Tu, K., Verma, S., Vesala, T., Wilson, K., and Wofsy, S.: Gap filling strategies for defensible annual sums of net ecosystem exchange, Agric. For. Meteorol., 107, 43–69, 2001.

Fan, S., Gloor, M., Mahlman, J., Pacala, S., Sarmiento, J., Takahashi, T., and Tans, P.: A large terrestrial carbon sink in North America implied by atmospheric and oceanic carbon dioxide data and models, Science, 282, 442–446, 1998.

FAO: World reference base for soil resources, Food and Agriculture Organization of the United Nations, Rome, available online at http://www.itc.nl/~rossiter/Docs/WRB/wsrr84e.pdf, 1998.

Gangoiti, G., Alonso, L., Navazo, M., Albizuri, A., Pérez-Landa, G., Matabuena, M., Valdenebro, V., Maruri, M., García J. A., and Millán M. M.: Regional transport of pollutants over the Bay of Biscay: analysis of an ozone episode under a blocking anticyclone in west-central Europe, Atmos. Environ., 36(8) 1349–1361, 2002.

Gangoiti, G., Millán, M. M., Salvador, R., and Mantilla E.: Long-range transport and re-circulation of pollutants in the western Mediterranean, during the project Regional Cycles of Air Pollution in the West-Central Mediterranean Area, Atmos. Environ., 35, 6267–6276, 2001.

Gerbig, C., Lin, J. C., Wofsy, S. C., Daube, B. C., Andrews, A. E., Stephens, B. B., Bakwin, P. S.,and Grainger, C. A.: Towards constraining regional-scale fluxes of CO_2 with atmospheric observations over a continent: 2. Analysis of COBRA data using a receptor-oriented framework, J. Geophys. Res., 108, 4757, doi:10.1029/2003JD003770, 2003.

Gioli B., Miglietta, F., De Martino, B., Hutjes, R. W. A., Dolman, H. A. J., Lindroth, A., Schumacher, M., Sanz, M. J., Manca, G., Peressotti, A., and Dumas, E. J.: Comparison between tower and aircraft-based eddy covariance fluxes in five European regions, Agric. For. Meteorol., 127, 1–16, 2004.

Gurney, K. R., Law, R. M., Denning, A. S., Rayner, P. J., Baker, D., Bousquet, P., Bruhwiler, L., Chen, Y.-H., Ciais, P., Fan, S., Fung, I. Y., Gloor, M., Heimann, M., Higuchi, K., John, J., Maki, T., Maksyutov, S., Masarie, K., Peylin, P., Prather, M., Pak, B. C., Randerson, J., Sarmiento, J., Taguchi, S., Takahashi, T., and Yuen, C.-W: Towards robust regional estimates of CO_2 sources and sinks using atmospheric transport models, Nature, 415, 626–630, 2002.

Hutjes, R., van den Bulk, W. C. M., Cosin, S., et al.: Regional Assessment and monitoring of the carbon balance within Europe (RECAB), Final Report. Alterra, PO Box 47, 6700 AC, Wageningen. Netherlands, 2003.

Kotroni, V., Kallos, G., Lagouvardos, K., Varinou M., and Walko, R.: Numerical Simulations of the Meteorological and Dispersion Conditions during an Air Pollution Episode over Athens, Greece, J. Appl. Meteorol., 38(4), 432–447, 1999.

Lin, J. C., Gerbig, C., Daube, B. C., Wofsy, S. C., Andrews, A. E., Vay, S. A., and Anderson, B. E.: An Empirical Analysis of the Spatial Variability of Atmospheric CO_2: Implications for Inverse Analyses and Space-borne Sensors, Geophys. Res. Lett., 31, L23104, doi:10.1029/2004GL020957, 2004.

Lu, L., Denning, A. S., da Silva-Dias, M. A., da Silva-Dias, P., Longo, M., Freitas, S. R., and Saatchi, S.: Mesoscale circulations and atmospheric CO_2 variations in the Tapajós Region, Pará, Brazil, J. Geophys. Res., 110, D21102, doi:10.1029/2004JD005757, 2005.

Marland, G., Boden, T. A., and Andres, R. J.: Global, regional, and national CO_2 emissions in trends: A compendium of data on global change, Carbon Dioxide Information Analysis Center, Oak Ridge National Laboratory, U.S. Department of Energy, Oak Ridge, Tenn., USA, 2003.

Michaelis, L. and Menten, M. L.: Die Kinetik der Invertinwirkung, Biochemische Zeitschrift, 49, 333–369, 1913.

Millán, M. M., Salvador, R., Mantilla, E., and Kallos, G.: Photooxidants dynamics in the Mediterranean basin in summer: Results from European research projects, J. Geophys. Res., 102(D7), 8811–8823, 1997.

Millán, M. M., Artiñano, B., Alonso, L., Castro, M., Fernandez-Patier, R., and Goberna, J.: Meso-Meteorological Cycles of Air Pollution in the Iberian Peninsula, (MECAPIP), Air Pollution Research Report 44, EUR No. 14834, European Commission DG XII/E-1, Rue de la Loi, 200, B-1040, Brussels, 1992.

Nicholls, M. E., Denning, A. S., Prihodko, L., Vidale, P. L., Davis, K., and Bakwin, P.: A multiple-scale simulation of variations in atmospheric carbon dioxide using a coupled biosphere-atmospheric model,. J. Geophys. Res., 109, D18117,

doi:10.1029/2003JD004482, 2004.

Olivier, J. G. J. and Berdowski, J. J. M.: Global emissions sources and sinks, in: The Climate System, edited by: Berdowski, J., Guicherit, R., and Heij, B. J., A. A. Balkema Publishers/Swets & Zeitlinger Publishers, Lisse, The Netherlands, ISBN 90-5809-255-0, 33–78, 2001.

Palau, J. L., Pérez-Landa, G., Diéguez, J. J., Monter, C., and Millán, M. M.: The importance of meteorological scales to forecast air pollution scenarios on coastal complex terrain, Atmos. Chem. Phys., 5, 2771–2785, 2005, http://www.atmos-chem-phys.net/5/2771/2005/.

Pérez-Landa, G., Ciais, P., Sanz, M. J., Gioli, B., Miglietta, F., Palau, J. L., Gangoiti, G., and Millán, M. M.: Mesoscale circulations over complex terrain in the Valencia coastal region, Spain – Part 1: Simulation of diurnal circulation regimes, Atmos. Chem. Phys., 7, 1835–1849, 2007, http://www.atmos-chem-phys.net/7/1835/2007/.

Rayner, P. J., Enting, I. G., Francey, R. J., and Langenfelds, R.: Reconstructing the recent carbon cycle from atmospheric CO_2, $\delta^{13}C$, and O_2/N_2 observations, Tellus, 51B, 213–232, 1999.

Schumacher, M.: Airborne and ground level flask sampling for regional carbon budgets the potential of multiple tracer and isotope analyses, PhD. thesis, University Hamburg, http://www.sub.uni-hamburg.de/opus/volltexte/2005/2576/, 2005.

Seufert, G., Sanz, M., and Millán, M. M.: Report on the 3rd BEMA measuring campaign at Burriana (Valencia–Spain) July 12–23, 1995, Joint Research Centre Rep. EUR 17305 EN (Available from Office of Official Publications of the European Communities, L-2985, Luxemburg), 140, 1997.

Tremback, C. J., Lyons, W. A., Thorson, W. P., and Walko, R. L.: An emergency response and local weather forecasting software system, Preprints, Eighth Joint Conf. on the Applications of Air Pollution, Nashville, TN, Amer. Meteorol. Soc., 219–233, 1994.

Walko, R. L., Tremback, C. J., and Bell, M. J.: HYPACT Hybrid Particle and Concentration Transport Model, Users Guide, Mission Research Corporation, Fort Collins, Colorado (USA), 2001.